Preprint
UCRL-JC-133053

Direct Observation of Phase Transformations in Austenitic Stainless Steel Welds Using In-Situ Spatially-Resolved and Time-Resolved X-Ray Diffraction

J.W. Elmer, J. Wong, T. Ressler

This article was submitted to
Second International Symposium on the Joining of Advanced Materials, ASM Materials Solutions '99, Cincinnati, OH, November 1-4, 1999

U.S. Department of Energy
Lawrence Livermore National Laboratory

September 23, 1999

Direct observation of phase transformations in austenitic stainless steel welds using in-situ spatially-resolved and time-resolved x-ray diffraction

by:
John W. Elmer, Joe Wong and Thorsten Ressler
Lawrence Livermore National Laboratory
University of California, P. O. Box 808, Livermore, CA, 94551

for:
The Second International Symposium on the Joining of Advanced Materials
ASM Materials Solutions '99, Cincinnati, Ohio, November 1-4, 1999

Abstract

Spatially resolved x-ray diffraction (SRXRD) and time resolved x-ray diffraction (TRXRD) were used to investigate real time solid state phase transformations and solidification in AISI type 304 stainless steel gas tungsten arc (GTA) welds. These experiments were conducted at Stanford Synchrotron Radiation Laboratory (SSRL) using a high flux beam line. Spatially resolved observations of $\gamma \leftrightarrow \delta$ solid state phase transformations were performed in the heat affected zone (HAZ) of moving welds and time-resolved observations of the solidification sequence were performed in the fusion zone (FZ) of stationary welds after the arc had been terminated. Results of the moving weld experiments showed that the kinetics of the $\gamma \rightarrow \delta$ phase transformation on heating in the HAZ were sufficiently rapid to transform a narrow region surrounding the liquid weld pool to the δ ferrite phase. Results of the stationary weld experiments showed, for the first time, that solidification can occur directly to the δ ferrite phase, which persisted as a single phase for 0.5s. Upon solidification to δ, the $\delta \rightarrow \gamma$ phase transformation followed and completed in 0.2s as the weld cooled further to room temperature.

Introduction

The microstructure of many AISI 300-series austenitic stainless steels consists of a mixture of austenite (γ) and delta ferrite (δ) phases [1-4]. Austenite, which is paramagnetic, has a face centered cubic (fcc) crystal structure, and is the predominant phase in these alloys. The remainder is ferrite, which is ferromagnetic and has a body centered cubic (bcc) crystal structure. The effects of alloy composition and weld solidification rate on the microstructure of austenitic stainless steel alloys have been extensively studied because residual ferrite in the microstructure can have both beneficial and deleterious effects on weld integrity. For example, the presence of a small amount of ferrite in welds is known to help reduce hot cracking [5-7], but the presence of ferrite can also result in reduced corrosion resistance [8,9] and reduced ductility under certain conditions [10-12].

The effect of composition on the phases that exist in arc welds was studied by Schaeffler more than 50 years ago [1] who developed a diagram to predict the amount of ferrite in stainless steel welds. This empirical diagram has been modified several times to enhance its accuracy [2-4]. The weld solidification rate further affects both the microstructure and the relative fraction of austenite and ferrite in welds [13-17]. Solidification rate studies such as these have been important in developing an understanding the effects that different welding processes have on the resulting fusion zone microstructure. However, the effect of welding on the HAZ microstructure is not as well understood. The phases that exist in the HAZ during welding at the fusion line are important factor in the evolution of microstructures in the fusion zone since the phases in the fusion zone are known to grow epitaxially from the liquid-solid interface in stainless steel welds [14].

In this investigation, direct observations of the ferrite and austenite phases were made during arc welding of an AISI type 304 stainless steel as a function of position in the HAZ using SRXRD and as a function of time using TRXRD. The SRXRD technique has recently been developed to investigate phase transformations in commercially pure titanium [18-21], while the TRXRD technique was developed earlier to elucidate chemical dynamics of fast, high temperature combustion synthesis reactions [22-24]. The goals of these experiments were twofold: first, to verify experimentally whether delta ferrite or austenite is the primary phase to solidify from the melt, and second to investigate if the kinetics of the $\gamma \rightarrow \delta$ phase transformation are sufficiently rapid for a complete or partial transformation during the transient weld heating cycle in the HAZ of arc welds.

Experimental Procedures

MATERIALS. AISI type 304 stainless steel was acquired in a 100 mm diameter bar. Chemical analysis was performed on this

material using combustion analysis for C, N, S and P, and inductively coupled plasma analysis for the remaining elements. The results yielded the following concentrations (in wt. %): 18.44% Cr, 10.71% Ni, 0.019% C, 0.053% N, 1.67% Mn, 0.04% Mo, <0.005%Nb, 0.46% Si, 0.04% V, 0.04% Cu, 0.02% Co, 0.016%S, 0.015% P, balance Fe (68.5%). The welded samples were inspected with optical microscopy by polishing the samples using standard metallographic procedures and etching the samples electrolytically in a 10% oxalic acid solution.

WELDING. Gas tungsten arc welds were made on the stainless steel bars using a 225 ampere maximum direct constant current welding power supply with electrode negative polarity. The welding electrode was made of W-2% Th and measured 4.7 mm diameter. A new electrode was used for each weld and was straight ground with a 60° included angle taper. The power was maintained constant at 1.8 kW (110 A, 16.7±0.5 V) for all of the welds. Helium was used as the welding and shielding gas, and a cross jet of helium was used to blow the evaporated metal powders away from the area where the x-ray diffraction measurements were being taken. These powders are largely composed of Fe, Mn and Cr, as shown by energy dispersive x-ray analysis in a scanning electron microscope. If these powders were allowed to react with the surface during welding, they would alter the chemistry and, hence, the phase com-position, of the surface. Thus, the cross jet of helium gas was necessary to prevent this problem.

Moving welds were made by rotating the stainless steel bar at a constant speed of 0.11 rpm below the fixed electrode. This resulted in a surface welding speed of 0.6 mm/s, which produced a 9.0 ± 0.25 mm wide fusion zone on the surface of the stainless steel bar. Stationary 'spot' welds were performed under the same welding conditions as the moving welds, but the bar was not rotated. The spot welds were terminated after about 15 s, when the weld pool had established a diameter of ~9mm. All welding was done inside an environmentally controlled chamber to minimize oxidation during welding. Prior to welding, the vacuum chamber was evacuated to less than 100 mTorr using a mechanical roughing pump and then back-filled with high purity (99.999%) helium gas. Further details on this welding chamber has been described in detail elsewhere [18,19].

SPATIALLY RESOLVED AND TIME RESOLVED DIFFRACTION. SRXRD and TRXRD measurements were performed on a 31-pole wiggler beam line, BL 10-2 [25] at SSRL with SPEAR (Stanford Positron-Electron Accumulation Ring) operating at an electron energy of 3.0 GeV and an injection current of ~100 mA. The synchrotron white beam emerging from the 31-pole wiggler was first focused by a toroidal mirror to the source size of ~1 × 2 mm, and then monochromatized with a double Si (111) crystal [18-21]. The focused monochromatic beam was then passed through a tungsten pinhole to render a sub-millimeter beam on the sample at an incident angle of ~25°. This setup yielded a beam flux on the sample of $\sim 10^{10}$ photons/s determined experimentally using an ion chamber immediately downstream from the pinhole. SRXRD experiments were performed using a 260μm pinhole to yield a spatial resolution of 300 μm on sample, and TRXRD experiments were performed with a 730μm pinhole to yield a proportionally higher photon flux to compensate for shorter integration times. Two photon energies were used: 12.0 keV (λ = 0.1033 nm) and 7.0 keV (λ = 0.1771 nm). The higher energy was used to maximize the number of Bragg peaks diffracting into the 2θ window for enhanced phase identification, and the lower energy was selected to be just below the Fe K-edge (7.112 keV [26]) to minimize the background contribution due to Fe K-fluorescence from the stainless steel samples

Diffraction patterns were recorded using a 50-cm long 2048-element position sensitive Si photodiode array detector. The detector and associated ST121 data acquisition system manufactured by Princeton Instruments were used to collect, store and display the x-ray diffraction data in real time. The array was mounted on a dual-stage Peltier effect cooler, which in turn was water-cooled. This detector was placed ~10 cm behind the weld to cover a 2θ range from 24° to 54°. At 12.0 keV, this 2θ range covers three δ-ferrite peaks: bcc (110), bcc(200), and bcc(211); and three γ-austenite peaks: fcc(111), fcc(200) and fcc(220). At 7.0 keV, only the 2 lower 2θ peaks of each phase appear in the window. Figure 1 shows the location of these 6 peaks for the respective powder patterns calculated at room temperature [27], for using lattice constants of 0.28665nm for bcc-Fe and 0.3666nm for fcc-Fe [28].

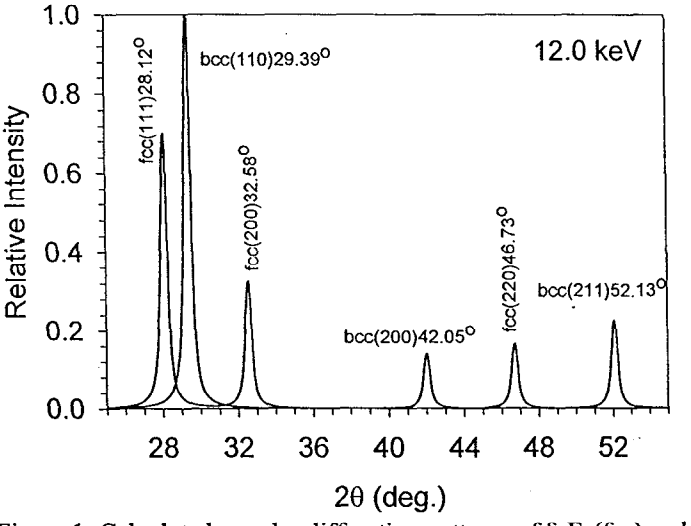

Figure 1: Calculated powder diffraction patterns of δ-Fe(fcc) and γ-Fe(fcc) showing locations of the 3 bcc and 3 fcc peaks in the 2θ window from 24° to 54° at 12.0 keV.

SRXRD data was taken on the *moving welds* by positioning the beam at a preset starting location with respect to the welding electrode. Diffraction patterns were then recorded during one revolution of the weld around the cylinder by incrementally jogging the weld in 250 μm steps to new locations and collecting diffraction intensities for 10 s at each location while the bar rotated under the torch at a constant speed. In this way a series of spatially resolved x-ray diffraction patterns was

collected, mapping the phases that exist in the HAZ along a line perpendicular to, and away from, the weld centerline.

TRXRD data was taken on the *stationary welds* by positioning the beam at a fixed distance from the center of the welding electrode and collecting data at 50 ms time intervals from the start to the end of the weld. In this case, a smaller number of grains are incorporated into the diffraction pattern than in the moving weld conditions because only one spot, rather than a strip, of material is inspected. The 730μm diameter pinhole was used to increase both the beam flux on sample and number of grains bathed by the synchrotron beam in order to achieve good signal to noise ratio of the observed diffraction peaks with a short integration time of 50 ms.

Results

PHASE EQUILIBRIA. The AISI 300-series stainless steels alloys are based on the Fe-Ni-Cr ternary system and have compositions that typically contain 65% to 70%Fe by weight [29]. The constitution of these alloys has been critically evaluated [30,31] and has provided the basis for understanding the effects of alloy composition and cooling rate on the microstructure of stainless steel welds. One useful way to visualize the relative amounts of austenite and ferrite as a function of temperature in these systems is through constant Fe isopleths [5, 13, 14, 32-34]. These diagrams can be used to predict solidification and solid state transformations in stainless steel alloys.

Figure 2 shows an isopleth through the Fe-Ni-Cr system at a constant Fe content of 68.5%Fe. This isopleth was calculated using ThermoCalc [35] to match the Fe content of the 304 stainless steel used in this investigation. This isopleth shows that ferrite is more stable at elevated temperatures than at room temperature, and that the phase transformation sequence during equilibrium solidification of these alloys varies with composition. For 304 stainless steel alloys that have Cr_{eq}/Ni_{eq} ratios near the line of two-fold saturation the solidification and solid state phase transformation sequence can be either $L\rightarrow(\delta+L)\rightarrow(\delta+\gamma+L)\rightarrow(\delta+\gamma)$ for Cr-rich alloys or, $L\rightarrow(\gamma+L)\rightarrow(\delta+\gamma+L)\rightarrow(\delta+\gamma)\rightarrow(\gamma)$ for Ni-rich alloys, where L refers to the liquid phase, δ refers to the bcc delta ferrite phase, and γ refers to the fcc austenite phase.

Arc-welded alloys that solidify with ferrite as the primary phase, i.e. $L\rightarrow(\delta+L)$ are known to have the best resistance to weld hot cracking [5], and thus it is desirable to have an alloy composition with a Cr_{eq}/Ni_{eq} ratio high enough to ensure primary ferrite solidification. Although these alloys solidify with a high volume fraction of ferrite that can approach 100%, these alloys typically contain only 5 to 8% residual ferrite in the microstructure after the weld has cooled to room temperature due to the solid state transformation of ferrite to austenite [5-7].

Based on the composition of the 304 stainless steel used in this investigation, the chromium equivalent was calculated to be Cr_{eq}=18.5 and the nickel equivalent was calculated to be Ni_{eq}= 12.4. These values were calculated using the WRC-1992 constitution diagram for stainless steel welds [4],

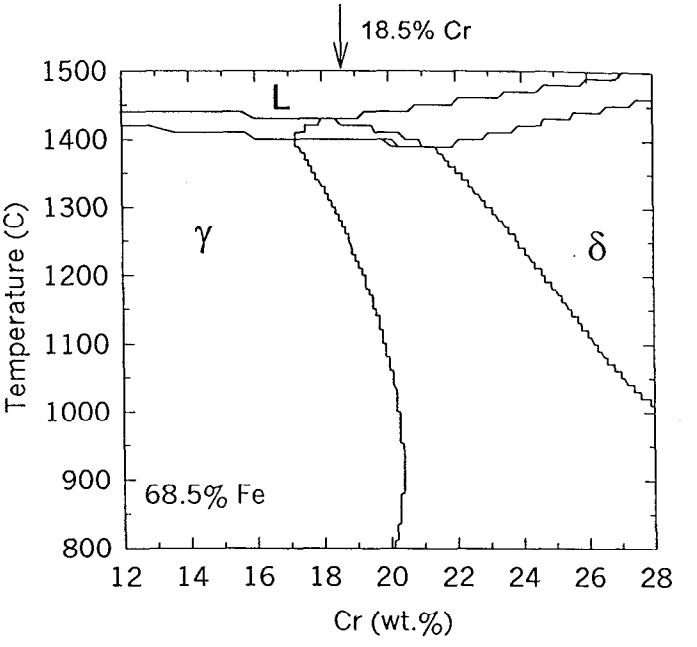

Figure 2: Isopleth through the Fe-Ni-Cr ternary system at 68.5% Fe as calculated by ThermoCalc. The composition of the 304 stainless steel used in this study (as estimated through chromium and nickel equivalents) is indicated by the arrow.

Where Ni_{eq}=Ni+35C+20N+0.25Cu, and Cr_{eq}=Cr+Mo+Nb. Thus, the Cr_{eq}/Ni_{eq} ratio of this alloy is 1.49, which lies close to, but on the Cr-rich side, of the line of two-fold saturation [7, 36]. Figure 2 indicates that this alloy should solidify with δ as the primary phase and should then continue through a mushy zone, which contains δ, γ and L. The ThermoCal results shown in Figure 2 indicate that the mushy zone should occur over a temperature range of 42 C° for this alloy composition.

The ferrite content of the GTA welds was measured using a Magne-Gage [37], showing that the base metal contained 0.36 wt% ferrite and that the weld metal contained 4.5% ferrite. These values represent an average of 6 readings each, and were performed on metallographically prepared flat surfaces. The retention of 4.5 wt% ferrite in the weld is sufficiently high to indicate that this alloy probably solidified with ferrite as the primary phase.

Figure 3 shows the results of optical metallography that was performed on the as welded samples by polishing the top surface of the weld in the same locations as the SRXRD measurements were taken. Figure 3a shows the HAZ region at low magnifications. Grain growth that occurred in the HAZ extends approximately 1mm from the fusion line into the base metal. The HAZ/fusion line microstructure is shown in Fig. 3b at a higher magnification. This view shows that the residual delta ferrite in the fusion zone dark etching phase has a curved vermicular morphology, which is an indication that this weld solidified in the primary ferrite mode [38]. Ferrite stringers extend approximately 200 μm from the fusion line into the HAZ.

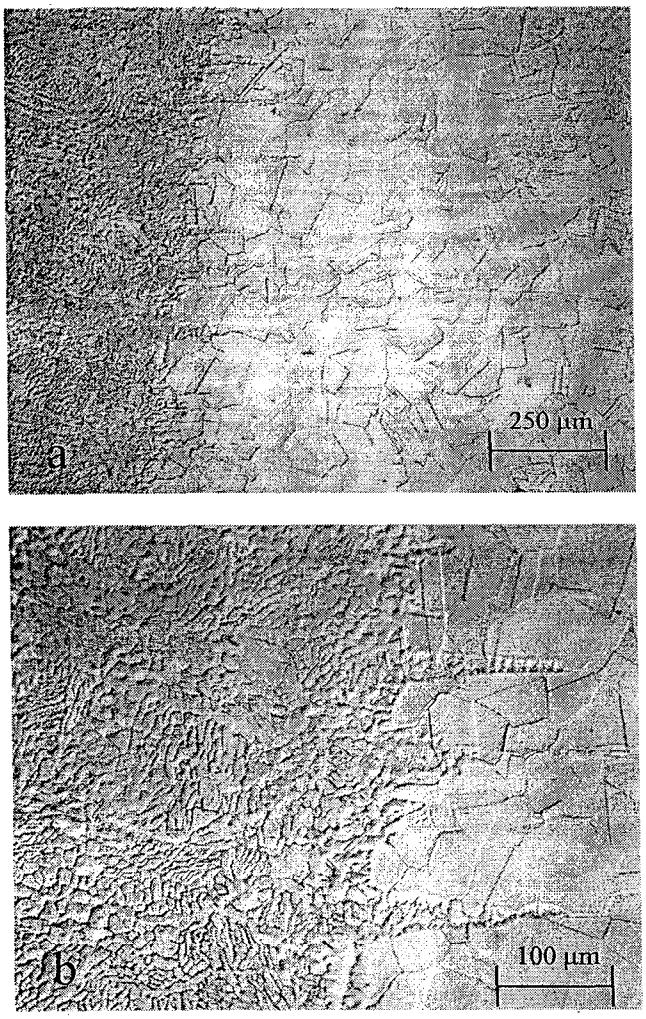

Figure 3: Microstructures of the fusion zone (left side of micrographs) and HAZ (right side of micrographs) of the welded 304 stainless steel. a) Grain growth region extending approximately 1mm into the HAZ, and b) curved vermicular morphology of the ferrite in the fusion zone, with ferrite stringers extending into the HAZ.

MOVING WELDS (phase mapping). Moving welds were performed by positioning the x-ray beam in a starting location 2.0 mm directly to the side of the electrode. This location was chosen so that the beam would be in the liquid weld pool immediately after the arc was struck, and as the experiment progressed, it would travel from the liquid weld pool and into the HAZ. Figure 4 shows a schematic drawing of the x-ray path as it was incrementally jogged to new positions during welding. A series of 36 locations were sampled with the beam at 0.25 mm increments, resulting in a 9.0 mm long path that was inspected. At each location a 10s integration time was used to collect a diffraction scan with a S/N ratio of ~300/1. Thus, a series of spatially resolved diffraction patterns was obtained along a given direction in the weld, which was then used to determine the phases present at each successive location in the HAZ *during welding*.

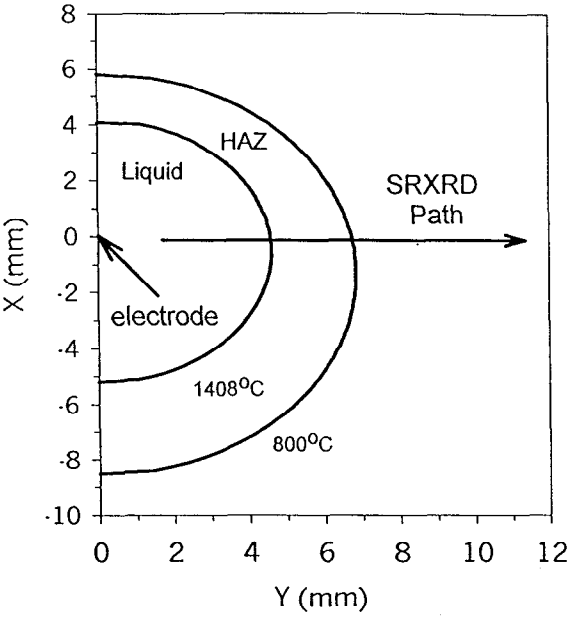

Figure 4: Schematic illustration of the SRXRD mapping sequence. The x-ray beam is initially positioned in the liquid weld pool at a location 2 mm from the electrode. The mapping sequence consists of 36 jogs at a spacing of 0.25 mm per jog, covering a total distance of 9 mm from the initial position. The melting point isotherm and 800°C isotherm are shown for reference, as calculated from the distributed heat source model.

Figure 5 shows the results of one of the SRXRD experiments on a moving weld. All 36 of the diffraction patterns are plotted from the starting position at Y=2mm to the ending position at Y=11 mm. The initial 7 diffraction patterns were taken while the X-ray beam was in the liquid pool, which yields no Bragg peaks. Here, we refer to a "frame" as one entire x-ray scan over the 30° range of 2θ. The first evidence of a solid crystalline phase appears in the eighth frame, where a small, but discernible, ferrite bcc(110) peak appears. The next three frames also contain only bcc peaks of various hkl relfections. In frame 12, the γ phase first appears and continues to persist in all of the remaining frames showing peaks for the fcc(111), fcc(200), and fcc(220) reflections. Coexistence of δ+γ phases appears in frames 12-14, as indicated by the presence of the bcc(110) peak with the γ peaks.

The occurrence of each of the diffraction peaks with respect to the location of the weld fusion line is summarized in Table 1. In this table, a cross indicates that a given peak was observed at the location. As the beam moved from the fusion line into the HAZ, δ ferrite diffraction peaks were observed over a total distance of 1.75 mm. In the latter 0.75 mm of this range δ coexisted with γ. This experiment was repeated two additional times with similar results in each of the three runs, whereby a single-phase δ region was observed immediately adjacent to the weld pool, and a δ+γ two-phase region was observed immediately outside of the δ region. Further away form the weld only the γ diffraction peaks were observed.

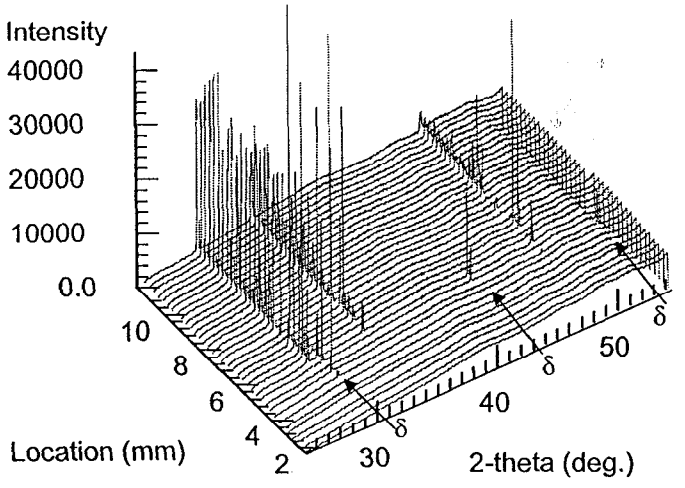

Figure 5: Spatially resolved x-ray diffraction patterns along the locations from Y= 2 mm to Y=11 mm at X = 2 mm from the liquid weld pool into the HAZ in 0.25 mm steps. All calculated hkl reflections for the δ and γ phase shown in Fig. 1 are observed. The first four frames exiting the liquid span 1.0 mm and are of the δ diffraction pattern only (indicated by arrows). A mixed δ+γ zone is then observed in the next 7 frames (1.75 mm). The remainder of the diffraction peaks, to 10.75 mm from the centerline of the weld, are the γ phase. This scan experiment was repeated two times with similar results in all three runs

Table 1: Location of the ferrite and austenite diffraction peaks for the moving welds shown in Fig. 5. The four frames in which only the bcc phase was observed are highlighted.

Frame	distance from FL (mm)	bcc 110	bcc 200	bcc 211	fcc 111	fcc 200	fcc 220
1-7	liquid						
8	0	x					
9	.25	x					
10	.50			x			x
11	.75	x	x				
12	1.0	x	x		x	x	x
13	1.25	x		x	x		
14	1.5	x			x	x	
15-36	1.75-7				x	x	x

Post weld measurements of the weld width showed that the fusion line oscillated by ± 0.25 mm from side-to-side due to oscillations of the liquid weld pool. Therefore, it is likely that the initial 2 frames (0.5 mm) where δ phase was observed as the beam moved into the HAZ were a time averaged mixture of liquid, the mushy region and the HAZ due to the variation in the fusion line position. After taking into account the variation in the liquid weld pool position (± 0.25mm), and the width of the mushy region (0.2 mm) as determined from the liquidus temperature range and the temperature gradient in the HAZ, it is likely that only 0.3 mm of the region where the δ phase diffraction peaks were observed in this run was obtained while the beam was entirely in the solid portion of the HAZ. Therefore, the experimentally measured δ region of the HAZ was estimated to be 0.3 mm wide. This width roughly corresponds to the length of the transformed ferrite stringers that appear in the HAZ.

The results of each of the three runs are summarized in Table 2, which shows the individual and average width of the single phase δ region and that of the δ+γ region as measured by SRXRD. These values have been corrected for the ± 0.25mm fluctuation of the weld pool boundary, but not the 0.2 mm wide mushy zone. These results indicate that δ was the first solid phase to be observed, and that it existed on average for 0.33 mm outside the liquid weld pool at this location. The δ+γ coexistence region extended past the single-phase δ region for an additional 1.66 mm on average

Table 2: Summary of the δ and δ+γ locations as measured by SRXRD with respect to the weld pool boundary for each of the three moving weld experiments.

	Run 1	Run 2	Run 3	Avg. (mm)
δ range (mm)	0.25	0.5	0.25	0.33
δ+γ range (mm)	1.0	2.75	1.25	1.66

STATIONARY WELDS (time resolved solidification). The stationary welds were performed by positioning the x-ray beam in the fusion zone at a fixed distance from the electrode. Thus, by clocking a series of diffraction patterns after terminating the arc, solidification of the fusion zone can be followed in real time as the weld pool cools. Due to the high cooling rate of the weld under these conditions, time resolved x-ray diffraction in the milli-seconds time domain was required to capture the solidification and associated solid state phase transformations as the weld pool cooled.

Figure 6 shows a series of TRXRD patterns recorded with a resolution of 50 ms during solidification of a stainless steel spot weld. After an initial period of featureless diffraction while the weld pool was liquid, bcc peaks of the δ-phase were observed as the first solid phase The δ-phase existed by itself for a period of 500ms (10 frames). The bcc peaks then persisted for an additional 200ms (4 frames) in coexistence with the fcc peaks of the γ phase. All three fcc peaks were observed in all of the remaining frames as the weld cooled to room temperature.

The results presented in Fig. 6 indicate that δ ferrite is the first phase to solidify from the liquid weld pool. To confirm this observation, the same experiment was repeated 10 additional times. The δ phase appeared first in 6 of these 10 additional experiments, while mixed δ+γ phases appeared in the other 4 experiments. Never were fcc peaks of the γ-phase observed by themselves as the first solid phase. In three of these experiments, some small intensity δ peaks co-existed with the γ peaks for up to 15 s after the arc had been terminated, but the majority of the transformation occurred in less than 1s.

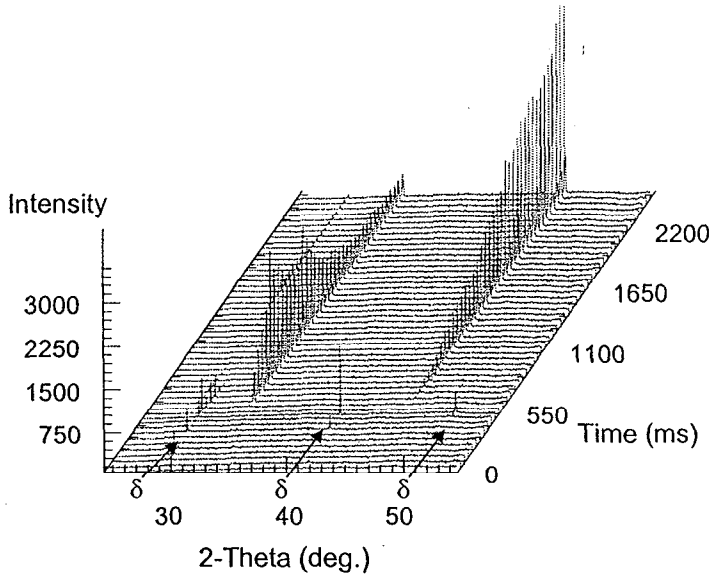

Figure 6. TRXRD patterns taken with a resolution of 50 ms during solidification of a stainless steel spot weld. The peaks (indicated by arrows) are the first to appear as solely the δ-phase for the first 500 ms. Coexistence of the δ and γ phases is observed during the next 200 ms followed by the appearance of all three fcc peaks of the γ-phase to room temperature. This experiment was reproducible five times with similar results

Discussion

MOVING WELDS. Understanding the thermal cycles in the FZ and HAZ is a pre-requisite for understanding microstructural evolution in the weldment since these temperature excursions cause phase transformations to occur. One computational method to estimate the temperature distribution around a moving weld is the distributed heat source (DHS) model which incorporates a generalized Gaussian distributed heat source [39-40] :

$$T = T_o + \left(\frac{\eta P}{\pi\rho c\sqrt{4\pi\alpha}}\right) * \int_0^t \left\{\left(\frac{1}{2\alpha t^{3/2} + \sigma^2 t^{1/2}}\right)\exp\left(\left(\frac{-(x-Vt)^2 + y^2}{4\alpha t + 2\sigma^2}\right) - \left(\frac{z^2}{4\alpha t}\right)\right)\right\} dt$$

In this equation, T is the temperature at a given set of spatial coordinates (x, y, z), P is the welding power, V is the welding speed, σ is the standard deviation of the Gaussian heat distribution, t is the transient welding time, η is the energy transfer efficiency (ratio of the power input to the workpiece to the power of the welding source), and T_0 is the initial temperature of the workpiece. The model assumes temperature independent values of the material properties where ρ is the density, c is the heat capacity at constant pressure, κ is the thermal conductivity, and α is the thermal diffusivity (α=κ/ρc).

The temperature distribution on the surface of the stainless steel bar (z=0) was calculated using the distributed heat source model for the welding conditions used in this study. In this calculation, the material properties for 304 stainless steel were estimated near its melting point of 1408°C to be: ρ=0.0078 g/mm^2, κ=0.035 W/mm-K, and c=0.689 J/g-K [41]. These calculations were performed with P=1800 W, V=0.6 mm/s, T_0=25°C, and a welding time of 60s. An energy transfer efficiency η=80% was chosen with a Gaussian distribution parameter σ=2 mm to match the actual weld pool width of 9 mm.

The results of the calculated temperatures are shown in Fig. 7, which plots the temperature distribution for the weld moving in the positive x-direction. In this plot, the temperature profile was truncated at the melting point of 1408°C to show the temperature distribution around the 9 mm diameter weld pool. The steep temperature gradients near the weld pool have peak values on the order of 100 C°/mm.

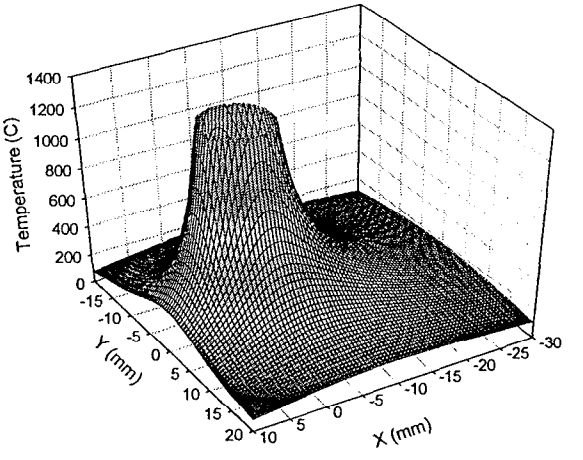

Figure 7: Surface plot of the calculated temperature distribution around the stainless steel weld moving in the positive x direction at a speed of 0.6 mm/s. The calculations are truncated at the melting point of 1408°C.

The region of the HAZ of most importance is near the liquid weld pool where the temperatures exceed about 800°C. This region is important because the diffusion-controlled transformation of austenite to ferrite is too slow at lower temperatures to allow phase transformations in stainless steels to occur during the relatively short welding time [42]. Fig. 4 compared the calculated melting point isotherm (1408°C) with the 800°C isotherm, showing the region in the HAZ where the diffusion controlled transformation between austenite and ferrite has sufficient time to occur. This region extends from the liquid weld pool at 4.5 mm from the centerline of the weld to 7 mm from the centerline of the weld, indicating that the portion of the HAZ where austenite-to-ferrite phase transformations is likely to occur has a maximum width of 2.5 mm.

From these calculations, the temperature profile along any given path can be made and compared with the SRXRD experimental results to provide a first order approximation to the temperatures that existed at the SRXRD locations. Figure 8 plots one of the calculated temperature profiles along the x-Ray

path at the X=0 position. This position is identical to that where the SRXRD data in Fig. 5 was taken. Superimposed on this plot are the locations where the δ, δ+γ, and γ phase regions as determined by the SRXRD experiments. The single-phase δ region extends 0.42 mm from the liquid pool, which corresponds to a temperature range from 1408°C to 1276°C as calculated by the DHS model. The mixed δ+γ phase region extends an additional 1.66 mm, which corresponds to a temperature range from 1276°C to 910°C. Therefore, these results show that along the X=0 path, which shows the effects of heating on the γ to δ phase transformation, peak temperatures of 1276°C or higher are required to completely transform the γ phase to the δ phase. Furthermore, temperatures above 910°C are required to partially transform γ to the δ, and no measurable transformation occurred during heating for peak temperatures below 910°C.

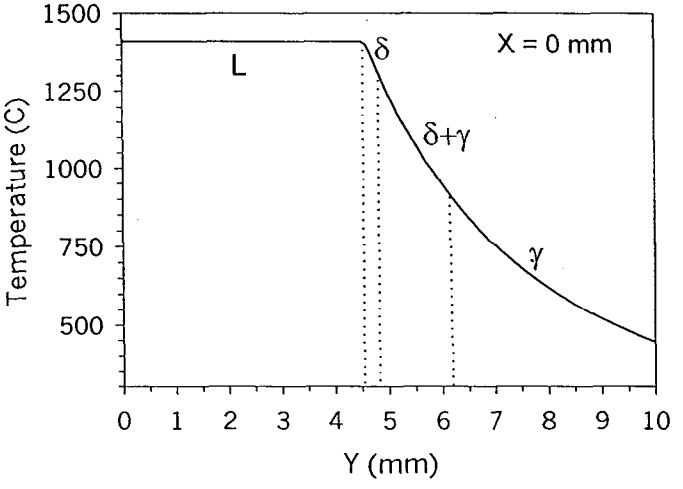

Figure 8: Calculated temperature profile for the moving weld in the y-direction and across the HAZ at the x=0 position where the SRXRD data was taken. The δ, δ+γ, and γ phase regions are indicated as identified by the SRXRD measurements, showing that δ-ferrite was present to temperatures as low as 910°C.

STATIONARY WELDS. The transient heating and cooling of the stationary welds was measured in a separate experiment by placing a thermocouple 6 mm from the center of the weld. The thermocouple used for this experiment was a 0.75 mm diameter sheathed type-k thermocouple, and was spring loaded in contact with the stainless steel bar.

The measured temperature profile for the spot weld is shown in Fig. 9, indicating that the peak heating and cooling rates were on the order of 450 C°/s, and that the temperature was approaching steady state value within about 10s of the arc initiation. The TRXRD data showed that the δ ferrite phase that solidified from the melt existed for 0.5 s before the γ phase was first observed. This cooling time corresponds to a temperature differential of about 225°C prior to the appearance of the γ phase. The mixed γ+δ region existed for an additional 0.2 s while δ transformed to γ, and during this time the weld would have cooled an additional 90°C. Therefore, the TRXRD measurements indicate that the majority of the δ ferrite phase would have transformed to γ by the time the weld reached a temperature of approximately 1100°C under the more rapidly cooling conditions of the spot welds.

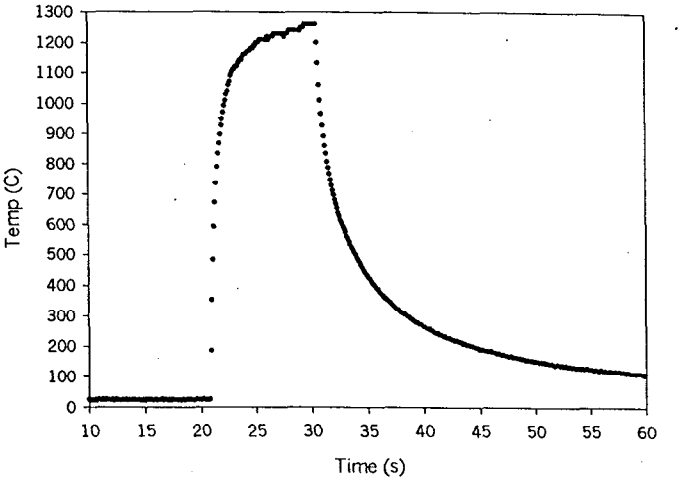

Figure 9: Transient temperature distribution around a spot weld in stainless steel as measured by a thermocouple placed 6 mm from the electrode.

Concluding Remarks

Spatially resolved diffraction measurements were made using a 300 μm synchrotron x-ray beam on sample to identify the phases present in the HAZ of AISI type 304 stainless steel GTA welds moving at 0.6 mm/s with a constant input power of 1.8 kW. These measurements showed that a single-phase region of δ-ferrite, 0.33 mm wide, existed adjacent to the liquid weld pool. A δ+γ coexistence region was determined to be 1.66 mm wide and located outside of the single-phase δ region. Using a distributed heat source model it was shown that peak temperatures of 1276°C or higher were required to reach the single-phase δ region, and that peak temperatures of 910°C or higher were required to bring about the γ → δ transformation

Time resolved diffraction measurements were also performed using a 730 μm synchrotron beam to identify the transformation dynamics of AISI type 304 stainless steel stationary 'spot' welds upon solidification and cooling to room temperature. Using a time resolution of 50 ms, these experiments showed directly, for the first time, that δ-ferrite is the first phase to solidify from the liquid weld pool. The δ-ferrite phase existed as the only solid phase for 0.5 s before beginning to transform to the γ–phase. The δ→γ transformation took an additional 0.2s of cooling, during which both phases co-exist. The cooling profile measured with a thermocouple showed that the cooling rate of these spot welds was on the order of 450 C°/s. The combined results showed that the majority of the δ-ferrite phase transformed to the γ–phase by the time the weld had reached a temperature of 1100°C or lower.

Acknowledgments

This work was performed under the auspices of the U. S. Department of Energy, Lawrence Livermore National Laboratory, under Contract No. W-7405-ENG-48. This work was supported by DOE, Office of Basic Energy Sciences, Division of Materials Science. Synchrotron experiments were conducted at SSRL supported by DOE, Division of Chemical Sciences. Thorsten Ressler, Fritz-Haber-Institute of the Max-Planck Society, Dept. of Inorganic Chemistry, Faradayweg 4-6, D-14195 Berlin, Germany, wishes to thank the Alexander von Humboldt Foundation for a Feodor Lynen research fellowship. The authors express gratitude to Dr. J. A. Brooks of Sandia National Laboratories for providing the stainless steel used in these experiments, Dr. S. Babu of Oak Ridge National Laboratory for performing Thermocalc calculations, Mr. A. T. Teruya of LLNL for writing LabView based software, Mr. B. Kershaw of LLNL for performing optical metallography, and Mr. J. Ferreira of LLNL for performing the SEM analysis.

References

1. A. L. Schaeffler," Constitution Diagram for Stainless Steel Weld Metal," *Metal Progress*, 56(11), p. 680, 1949.
2. C. J. Long and W. T. DeLong, "The Ferrite Content of Austenitic Stainless Steel Weld Metal," *Welding Journal*, 52(7), p. 281-s, 1973.
3. T. A. Siewart, C. N. McCowan, and D. L. Olson, "Ferrite Number Prediction to FN100 in Stainless Steel Weld Metal," *Welding Journal*, 67(12), p. 289-s, 1988.
4. D. J. Kotecki and T. A. Siewart, "WRC-1992 Constitution Diagram for Stainless Steel Weld Metals: A Modification of the WRC-1988 Diagram," *Welding Journal*, 71(5), p. 171-s, 1992.
5. J. A. Brooks and A. W. Thompson, "Microstructural Development and Solidification Cracking Susceptibility of Austenitic Stainless Steel Welds," *Int. Met. Reviews*, 36(1), p. 16, 1991.
6. J. C. Lippold, "Solidification Behavior and Cracking Susceptibility of Pulsed-Laser Welds in Austenitic Stainless Steels," *Welding Journal*, 73(6), p. 129-s, 1994.
7. S. Katayama, T. Fujimoto and A. Matsunawa, "Correlation among Solidification Process, Microstructure, Microsegregation and Solidification Cracking Susceptibility in Stainless Steel Weld Metals," *Transactions of JWRI*, 14(1), p. 123, 1985.
8. M. O. Malone, "Sigma and 885F Embrittlement of Chromium-Nickel Stainless Steel Weld Metals," *Welding Journal*, 46(6), p. 241-s, 1967.
9. H. Y. Yan and Z. Sun," Development of Welding Wire for High Purity Austenitic Stainless Steels," *Welding Journal*, 78(2), 38-s, 1999.
10. R. Viswanathan, J. I. Nurminen and R. G. Aspden,"Stress Corrosion Behavior of Stainless Steel Welds in High Temperature Water Containing Chloride," *Welding Journal*, 58(4), 118-s, 1979.
11. T. A. Whipple, H. I. McHenry and D. T. Read, "Fracture Behavior of Ferrite-Free Stainless Steel Welds in Liquid Helium," *Welding Journal*, 60(4), 72-s, 1981.
12. D. T. Read, H. I. McHenry, P. A. Steinmeyer and R. D. Thomas, Jr.," Metallurgical Factors Affecting the Toughness of 316L SMA Weldments at Cryogenic Temperatures," *Welding Journal*, 59(4), 104-s, 1980.
13. S. A. David, J. M. Vitek and T. L. Hebble, " Effect of Rapid Solidification on Stainless Steel Weld Metal Microstructures and it's Implications on the Schaeffler Diagram," *Welding Journal*, 66(10), p. 289-s, 1987.
14. J. W. Elmer, S. M. Allen, and T. W. Eagar, "Microstructural Development During Solidification Of Stainless Steel Alloys," *Metall. Trans. A* 20A (10), p 2117, 1989.
15. J. W. Elmer, T. W. Eagar, "The Influence Of Cooling Rate On The Ferrite Content Of Stainless Steel Alloys," *Recent Trends In Welding Science and Technology*, edited by S. A. David and J. M. Vitek, American Society for Metals, p 165, 1990.
16. J. W. Yardy and B. N. Laursen, "Microstructural Predictions for Laser Welded Austenitic Stainless Steels," *Trends in Welding Research, , Pine Mountain Georgia*, edited by J. M. Vitek et al., American Society for Metals, p. 89, 1998.
17. S. Katayama, T. Iamboliev and A. Matsunawa, "Formation Mechanism of Rapidly Quenched Microstructure of Laser Weld Metals in Austenitic Stainless Steel," *Trends in Welding Research, Pine Mountain Georgia*, edited by J. M. Vitek et al., American Society for Metals, p. 93, 1998.
18. Thorsten Ressler, Joe Wong and J. W. Elmer, "Investigation of Real-Time Microstructure Evolution in Steep Thermal Gradients using Spatially Resolved X-ray Diffraction: A Case Study for Ti Fusion Welds," *J. Phys. Chem. B*, 12(10), p. 102, 1998.
19. J. W. Elmer, Joe Wong and Thorsten Ressler, "Spatially Resolved X-Ray Diffraction Phase Mapping and $\alpha \rightarrow \beta \rightarrow \alpha$ Transformation Kinetics in the HAZ of Commercially Pure Titanium Arc Welds," *Metall. and Mater. Trans. A*, 29A(11), p. 2761, 1998.
20. J. W. Elmer, Joe Wong, M. Fröba, P. A. Waide, and E. M. Larson, "Analysis of Heat Affected Zone Phase Transformations Using In-Situ Spatially Resolved X-Ray Diffraction With Synchrotron Radiation," *Metall. and Mater. Trans. A*, 1996, 27A(3), p. 775.
21. Joe Wong, M. Fröba, J. W. Elmer, P. A. Waide, and E. M. Larson, "In Situ Phase Mapping and Transformation Study in Fusion Welds," *J. Mater. Sci.*, 32, p. 1493,1997.
22. Joe Wong, E. M. Larson, J.B. Holt, P.A. Waide, B. Rupp, R. Frahm ,"Time-resolved diffraction study of solid combustion reactions," *Science* vol. 249, 1406, 1990.
23. E. M. Larson, P. A. Waide and Joe Wong, " High speed diffractometer reaction chamber using synchrotron radiation," *Rev. Sci. Instrum.*, vol 62 (1), 53-7, 1991.
24. E.M. Larson, Joe Wong, J.B. Holt, P.A. Waide, B. Rupp and L.J.Terminello "A Time-resolved Diffraction Study of the Ta-C Combustion System," J. Mat. Res. vol. 8, 133, 1993.
25. V. Karpenko, J.H. Kinney, S. Kulkarni, K. Neufeld, C.

Poppe, K.G. Tirsell, Joe Wong, J. Cerino, T. Troxel, J. Yang, E. Hoyer, M. Green, D. Humpries, S. Marks, and D. Plate: *Rev. Sci. Instrum.*, 1989, 60, pp. 1451-1460.
26. A. Bearden and A. F. Burr: *Rev. Mod. Phys.*, 1967, vol. 39, pp. 125-37.
27. *PowderCell, v. 1.0,* Federal Institute for Materials Research and Testing, Rudower Chaussee 5, 12489 Berlin, Germany.
28. Pearson's Handbook, Crystallographic Data for Intermetallic Phases, Vol. 3, *ASM International*, 1985.
29. Metals Handbook, Ninth Edition, Vol. 3, *ASM International*, 1979.
30. V. G. Rivlin and G. V. Raynor," Phase Equilibria in Iron Ternary Alloys 1: Critical Evaluation of Constitution of Chromium-Nickel-Iron System," *Int. Met. Reviews*, 1, p. 21, 1980.
31. E. Schurmann and J. Brauckmann, "Investigations of the Melting Equilibria in the Iron Corner of the Ternary System Fe-Cr-Ni," *Arch. Eisenhuttenwes*, 48(a), p. 13, 1977.
32. J. C. Lippold and W. F. Savage, "Solidification of Austenitic Stainless Steel Weldments: Part 2- The Effect of Alloy Composition on Ferrite Morphology," W*elding Journal*, 59(2), p. 48-s, 1980.
33. ASM Handbook, Vol. 6, Welding, Brazing and Soldering: J. A. Brooks, J. C. Lippold, "Selection of Wrought Austenitic Stainless Steels,"*ASM International*, p. 456, 1993.
34. J. A. Brooks, J. C. Williams and A. W. Thompson, "STEM Analysis of Primary Austenite Solidified Stainless Steel Welds," *Metall. Trans. A*, 14(1), p. 23, 1983.
35. ThermoCalc calculations were performed by Dr. S. Babu, Oak Ridge National Laboratory, April, 1999.
36. T. Takalo, N. Suutala and T. Moisio, "Austenitic Solidification Mode in Austenitic Stainless Steel Welds," *Metal. Trans. A*, 10(8), p. 1173, 1979.
37. E. Stalmasek, "Measurement of Ferrite Content in Austenitic Stainless Steel," WRC Bulletin 318, 1986.
38. S. A. David, "Ferrite Morphology and Variations in Ferrite Content in Austenitic Stainless Steel Welds," Welding Journal, 60(4), p. 63-s, 1981.
39. T. W. Eagar and N. S. Tsai: *Welding Journal*, 1983, 62(12), pp. 346s-355s.
40. H. E. Cline and T. R. Anthony: *Journal of Applied Physics*, 1977, 48(9), pp. 3895-3900.
41. Y. S. Touloukian and C. Y. Ho: *Thermophysical Properties of Matter*, Plenum Press, New York, 1972.
42. J. M. Vitek, S. A. David, and S. A. Vitek," Modeling the Ferrite-to-Austenite Transformation in the Heat Affected Zone of Stainless Steel Multi-Pass Welds," *Trends in Welding Research, Proceedings of the 4th International Conference,* edited by Smartt, Johnson and David, American Society for Metals, p 223, 1996.